Research Square

Preprints are preliminary reports that have not undergone peer review.
They should not be considered conclusive, used to inform clinical practice,
or referenced by the media as validated information.

Pseudocapacitive Behavior and Efficient Energy Storage Mechanism of Bamboo Powder-Based Porous Carbon Synergistically Modified by FeCl3-MoS2

Shuaifei Li
Jilin Jianzhu University
Mingshu Chi
cms20062006@163.com

Jilin Jianzhu University
Li Bai
Jilin Jianzhu University
Xianbo Song
Jilin Jianzhu University
Yongjia Wu
Jilin Jianzhu University
Cong Zhang
Jilin Jianzhu University
Jinlong Qiao
Jilin Jianzhu University
Jingkai Li
Jilin Jianzhu University

Short Report

Keywords: Bamboo powder-derived porous carbon, FeCl3-MoS2 synergistic modification, Hierarchical pore structure, Pseudocapacitance, Defect regulation, Supercapacitor

Posted Date: September 4th, 2026

DOI: https://doi.org/10.21203/rs.3.rs-10785248/v1

License: This work is licensed under a Creative Commons Attribution 4.0 International License.
Read Full License

Additional Declarations: No competing interests reported.

Abstract

To overcome the defects of single MoS_2-modified biomass carbon including sheet agglomeration, slow electron transfer and inadequate pseudocapacitive sites, a hydrothermal-KOH activation method was developed to synthesize $FeCl_3$-MoS_2 co-modified hierarchical porous carbon (BPCM) from moso bamboo powder. $FeCl_3$ serves as a multi-functional agent to create pores, induce MoS_2 defects and generate Fe redox sites, cooperating with MoS_2 to form a 3D interconnected micro-mesoporous honeycomb framework. The optimized BPCM-1-2-800 (1.0 M $FeCl_3$, carbon/KOH mass ratio 1:2, 800°C) possesses a high BET surface area of 2164.37 $m^2 g^{-1}$. XRD, Raman, SEM-EDS and XPS verify uniform Fe, Mo, S distribution and in-situ FeS formation that enrich active sites and boost electron transport. In 6 M KOH three-electrode tests, BPCM-1-2-800 reaches 450 F g^{-1} at 0.5 A g^{-1} with 95% capacitance retention after 5000 cycles. The assembled symmetric two-electrode device delivers 242 F g^{-1} at 0.5 A g^{-1}, a peak energy density of 28.6 Wh kg^{-1} at 250 W kg^{-1} and 92.3% cycling retention over 10000 cycles. The outstanding performance stems from the synergy of hierarchical pores, Fe/Mo Faradaic reactions and conductive carbon networks. This study offers a cheap, green and scalable strategy for high-performance biomass supercapacitor electrodes.

1 Introduction

Driven by global climate change and the over consumption of fossil fuels, the world energy system is undergoing an accelerating shift toward renewable and clean energy sources[1]. Biomass energy has garnered widespread attention due to its remarkable renewability, substantial carbon neutrality potential, and pivotal role in advancing the circular economy, making it a potent alternative to traditional energy sources and a core pillar of low-carbon sustainable development[2]. As a key branch of electrochemical energy storage technology, supercapacitors (SCs) have become indispensable in advanced energy storage systems owing to their ultrahigh power density, exceptional cycling stability, fast charge–discharge kinetics, and long service life[3]. According to their energy storage mechanisms, supercapacitors are mainly divided into electrical double-layer capacitors (EDLCs) and pseudocapacitors (PCs). EDLCs store charges through physical ion adsorption-desorption at the electrode/electrolyte interface, exhibiting superior stability and long cycle life, whereas PCs rely on reversible Faradaic reactions to provide much higher specific capacitance[4].

Among numerous electrode materials, biomass-derived porous carbon has become a research hotspot for supercapacitor electrodes due to its abundant sources, low cost, excellent chemical stability, and tunable pore structure[5]. Converting low-cost biomass waste into high-value porous carbon electrodes carries substantial economic and environmental benefits[6]. Molybdenum disulfide, a typical two-dimensional transition metal dichalcogenide (TMD), features a graphene-like layered structure, large specific surface area, and rich redox activity, making it an ideal candidate to enhance the PCs of carbon materials[7]. Nevertheless, the inherent semiconductor properties and easy stacking of pure MoS_2 severely limit its conductivity and active site exposure[8]. Fe-based compounds have been proven to

effectively regulate the pore structure of carbon materials, induce defect engineering in MoS_2, and introduce additional Fe-based redox pseudocapacitive centers[9, 10]. Therefore, the rational construction of a $FeCl_3$-MoS_2 synergistic modification system is expected to break through the performance limitations of single modification, realize the collaborative optimization of pore structure, conductivity, active sites, and structural stability, and significantly boost the pseudocapacitive behavior and overall energy storage properties of biomass-derived porous carbon. Extensive studies on MoS_2-biochar composites have been reported. K. Krishnamoorthy et al. showed that the MoS2/Mo electrode provided a specific capacitance of approximately 192.7 F g^{-1} at a current density of 1 mA/cm^2 through constant current charge-discharge analysis[11]. Wang et al. fabricated flower-like three-dimensional MoS_2 microspheres constructed by nanoflakes, which at a current density of 1 A g^{-1} attained a specific capacitance of 518.7 F/g[12]. However, traditional biomass-derived carbon and its conventional MoS_2-modified composites still face prominent bottlenecks that restrict their application in high-power supercapacitors: (1) the intrinsic low conductivity of MoS_2 leads to high internal resistance and sluggish electron transfer; (2) MoS_2 nanosheets tend to agglomerate during preparation and detach from the carbon matrix during long-term cycling, resulting in rapid performance decay; (3) single-component modification or simple physical compounding fails to synchronously regulate the carbon pore structure, MoS_2 microstructure, and surface active sites; (4) Fe-based reagents are mostly used as single dopants, and their multi-effects as pore-forming agents and structure-directing agents, as well as the inter-component synergistic mechanism, remain unclear.

To overcome the above bottlenecks, this work proposes a novel hydrothermal-assisted $FeCl_3$/MoS_2 co-modification strategy using moso bamboo powder as the biomass precursor to prepare high-performance porous carbon electrodes. In this system, $FeCl_3$ acts as a multifunctional regulator: it constructs a hierarchical micro/mesoporous network as a pore-forming agent, optimizes the defect structure and electronic state of MoS_2 through defect engineering, and introduces Fe-based redox sites to enhance pseudocapacitance. The synergistic coupling of $FeCl_3$ and MoS_2 effectively improves the conductivity, inhibits the agglomeration of MoS_2, and maximizes the exposure of active sites. By systematically regulating the preparation parameters including $FeCl_3$ concentration, KOH activation ratio, and temperature, the optimal sample BPCM-1-2-800 exhibits a superhigh specific surface area, developed hierarchical pores, low internal resistance, and outstanding electrochemical performance. This study systematically elucidates the synergistic enhancement mechanism of pore structure, defect regulation, and pseudocapacitance, and provides a green, low-cost, and scalable approach for the design and preparation of high-performance biomass-derived carbon electrodes for advanced supercapacitors.

2 Experiment and Materials

2.1 Materials

Moso bamboo was collected from Guangde, Anhui Province, China, and ground into 60-mesh bamboo powder for subsequent use. All chemical reagents were of analytical grade and used as received without further purification. Molybdenum disulfide (MoS_2), ferric chloride hexahydrate ($FeCl_3·6H_2O$), potassium hydroxide (KOH), hydrochloric acid (HCl), acetylene black, polyvinylidene fluoride (PVDF), and N-methyl-2-pyrrolidone (NMP, 98%) were purchased from Shanghai Macklin Biochemical Technology Co., Ltd., China.

2.2 Preparation of $FeCl_3$-MoS_2 Co-Modified Bamboo-Derived Porous Carbon

Bamboo powder was used as the carbon source. Typically, 4 g of bamboo powder was uniformly mixed with 0.6 g of MoS_2 powder, followed by the addition of 50 mL $FeCl_3$ solution with different concentrations (0.5 M, 1.0 M, and 1.5 M). The mixture was transferred into a 100 mL Teflon-lined stainless-steel autoclave and heated at 180°C for 6 h under a nitrogen flow of 60 mL min^{-1} to achieve hydrothermal carbonization and in-situ Mo/S doping. After cooling to room temperature, the solid product was filtered and washed with deionized water until the filtrate was neutral (pH = 6.8 ± 0.2). The obtained sample was dried at 90°C for 12 h and denoted as BPCM-x, where x represents the molar concentration of $FeCl_3$. For further activation, BPCM-x was mixed with KOH at mass ratios of 1:1, 1:2, 1:3, and 1:4 (hydrothermal carbon: KOH). The mixture was immersed in deionized water for 2 h and magnetically stirred for 1 h to ensure homogeneous impregnation. After removing excess water, the sample was dried at 90°C for 12 h and activated in a tube furnace at 700°C 800°C, or 900°C for 2 h under nitrogen atmosphere with a heating rate of 10°C min^{-1}. After cooling naturally, the product was ground, washed with 1 M HCl to remove impurities, and rinsed with deionized water until neutral. Finally, the sample was dried at 90°C for 12 h to obtain the final porous carbon, labeled as BPCM-x-y-z, where "y" represents the mass ratio of potassium hydroxide to BPCM-x sample, and z represents the activation temperature.

2.3 Structural characterization

N_2 adsorption–desorption isotherms were measured at 77 K using a Tristar II 3020 surface area analyzer (Micromeritics, USA). The specific surface area (SSA) was calculated by the Brunauer–Emmett–Teller (BET) method, and pore size distribution (PSD) was determined via the density functional theory (DFT) method. Mesopore parameters were calculated using the Barrett–Joyner–Halenda (BJH) method.Raman spectra were collected on a HORIBA HR Evolution spectrometer with a 633 nm laser. X-ray diffraction (XRD) patterns were recorded on a Bruker D8 Advance diffractometer (Germany) with Cu Kαradiation (λ = 1.5406 Å). Morphology and microstructure were observed using a Hitachi S-4800 field-emission scanning electron microscope (SEM). Elemental mapping was performed via energy-dispersive X-ray spectroscopy (EDS, Oxford X-Max, UK).X-ray photoelectron spectroscopy (XPS) was conducted on a Thermo Fisher ESCALAB 250Xi+ system. All spectra were calibrated using the C 1s peak at 284.8 eV.

2.4 Electrochemical Experiment

Electrochemical tests were performed on a Versa STAT 4 electrochemical workstation at room temperature using a standard three-electrode system. The working electrode was fabricated by mixing the as-prepared porous carbon, acetylene black, and PVDF binder at a mass ratio of 8:1:1 in NMP. The homogeneous slurry was coated onto 1×1 cm² nickel foam, dried at 90°C, and pressed at 20 MPa for 2 min. The mass loading of active material was approximately 5 mg cm^{-2}.

The 6 M KOH solution was used as the electrolyte, a saturated calomel electrode (SCE) as the reference electrode, and a platinum foil as the counter electrode. Cyclic voltammetry (CV) was tested at scan rates of 5-100 mV s^{-1} in a potential window of -1.0 to 0 V. Galvanostatic charge–discharge (GCD) measurements were carried out at current densities from 0.5 to 20 A g^{-1}. Electrochemical impedance spectroscopy (EIS) was performed in the frequency range of 0.01 Hz to 10^4 Hz with an AC amplitude of 5 mV. The specific capacitance (Cs, F g^{-1}) of the porous carbon electrode prepared in the three-electrode system is determined from the GCD curve using Eq. (1).

$$C = \frac{I \times \Delta t}{m \times \Delta V} \tag{1}$$

where I (A) is the discharge current, Δt (s) is the discharge time, m (g) is the mass of active material, and ΔV (V) is the potential window.

For practical device evaluation, symmetric two-electrode supercapacitors were assembled by sandwiching a porous carbon soaked with 6 M KOH electrolyte between two identical working electrodes (1×1 cm²). The device specific capacitance (C_{device}), energy density (E) and power density (P) were calculated via Equations (2)–(4), as shown below:

$$C_{device} = \frac{I \times \Delta t}{2 \times m \times \Delta V} \tag{2}$$

$$E = \frac{C_{device} \times \Delta V^2}{2 \times 3.6} \tag{3}$$

$$P = \frac{3600 \times E}{\Delta t} \tag{4}$$

where m represents the mass of active material on a single electrode.

3 Results and Discussion

3.1 Analysis of the specific surface area and pore structure of BPCM-x

The nitrogen adsorption-desorption isotherms and pore size distributions of the $FeCl_3/MoS_2$ co-modified bamboo-based porous carbon samples BPCM-x were systematically investigated, as presented in Fig. 1.

All isotherms measured at 77 K displayed a steep adsorption rise at low relative pressure ($P/P_0 < 0.1$) and obvious hysteresis loops at high relative pressure, which can be classified as typical type I/IV composite isotherms (Fig. 1a). The intensive adsorption at low pressure confirmed the dominant microporous feature, whereas the adsorption platform observed at $P/P_0 \approx 0.2$ verified the coexistence and synergistic effect of micropores and mesopores[13].

Comparative analysis revealed that BPCM-1-2-800 and BPCM-1.5-2-800 exhibited significantly higher nitrogen adsorption capacities than BPCM-0.5-2-800, suggesting larger specific surface areas (SSAs) and more developed porous architectures[14]. This result validates that a moderate increase in $FeCl_3$ concentration can strengthen the pore-forming effect of MoS_2 within the porous carbon matrix. Nevertheless, the adsorption capacity of BPCM-1.5-2-800 was lower than that of BPCM-1-2-800, demonstrating that an excessive $FeCl_3$ dosage degrades the pore structure. This phenomenon can be ascribed to the magnetic agglomeration of Fe-based species (which weakens catalytic activity) and the intensified catalytic graphitization of amorphous carbon triggered by $FeCl_3$, both of which block partial pores and induce the collapse of micropores[15]. Quantitative pore structure parameters further supported these tendencies. The SSAs of BPCM-0.5-2-800, BPCM-1-2-800 and BPCM-1.5-2-800 were 1200.78, 2164.37 and 1731.45 $m^2 g^{-1}$, with total pore volumes of 0.542, 0.951, and 0.742 $cm^3 g^{-1}$, respectively. Regarding the surface area distribution, micropores contributed 45.5%, 82.5%, and 82.3%, while mesopores accounted for 54.5%, 17.5% and 17.7%, respectively. For pore volume proportions, micropores occupied 21.2%, 39.4% and 40.0%, whereas mesopores held 78.8%, 60.6%, and 60.0%. At a low $FeCl_3$ concentration (BPCM-0.5-2-800), the interaction between $FeCl_3$ and MoS_2 triggered selective etching, favoring the formation of mesopores. In contrast, BPCM-1-2-800 and BPCM-1.5-2-800 underwent intense oxidative etching of the carbon framework, producing abundant micropores. The slightly higher micropore volume in BPCM-1.5-2-800 may arise from the collapse of pore walls and the fusion of mesopores caused by excess $FeCl_3$, which reduces mesopore content while promoting micropore generation. $FeCl_3$ and MoS_2 acted as synergistic structure-directing agents, constructing a hierarchical micro-mesoporous network in bamboo-derived carbon that markedly accelerates ion transport kinetics[16]. Such a well-tuned porous structure exposes abundant electrochemically active sites, laying a solid foundation for outstanding supercapacitor performance. The pore size distribution curves (Fig. 1b) further confirmed that all samples were dominated by micropores and mesopores. Collectively, the $FeCl_3/MoS_2$ synergistic modification coupled with high-temperature KOH activation enables effective regulation over the pore structure of biomass-derived porous carbon, showing excellent feasibility and effectiveness.

To investigate the influence of $FeCl_3$ concentration on the supercapacitive performance of moso bamboo-derived porous carbon, electrochemical measurements were carried out using a standard three-electrode configuration. At a scan rate of 20 mV s^{-1}, the CV curves of all samples displayed quasi-rectangular shapes (Fig. 2a), revealing dominant electric double-layer capacitive behavior. BPCM-1-2-800 showed the most regular rectangular profile and the largest integrated area, verifying its superior

capacitive performance benefited from efficient ion diffusion and adsorption within its hierarchical porous structure. The GCD curves recorded at 0.5 A g^{-1} (Fig. 2b) exhibited symmetric triangular shapes with no obvious voltage drop, demonstrating highly reversible charge-discharge behavior[17]. Notably, BPCM-1-2-800 possessed the longest charge-discharge duration, corresponding to the highest specific capacitance. EIS analysis (Fig. 2c) illustrated that BPCM-1-2-800 possessed the smallest semicircle diameter (representing the lowest charge-transfer resistance) and a slope nearly close to 90°, indicating the closest approach to ideal capacitive response[18]. Furthermore, BPCM-1-2-800 displayed the lowest voltage drop at current densities ranging from 0.5 to 20 A g^{-1} (Fig. 2b), suggesting ultra-low internal resistance and fast charge transport kinetics. The outstanding electrochemical performance of BPCM-1-2-800 is mainly ascribed to its interconnected 3D hierarchical porous architecture (Fig. 4b), which effectively promotes charge transfer and lowers transport resistance[19]. In summary, these results demonstrate that 1.0 M $FeCl_3$ is the optimal concentration for preparing high-performance bamboo-derived porous carbon electrodes.

3.2 Physical property characterization of BPCM-x

The graphitization degree and crystalline features of the as-prepared bamboo-derived porous carbons were analyzed by X-ray diffraction (XRD). As displayed in Fig. 3a, BPCM-1-2-800, BPCM-1-3-800, and BPCM-1-4-800 show almost identical diffraction patterns. Distinct diffraction peaks at 2θ = 21.341°, 30.960°, 35.626°, 37.088°, and 40.415° are well indexed to the (111), (022), (200), (040), and (212) crystal planes of K_2SO_4 (PDF#05-0613), which originates from the reaction between K^+ (released during KOH activation) and SO_4^{2-} (generated by MoS_2 oxidation), in good agreement with the sulfate signals observed in the XPS analysis. A broad diffraction peak located at 2θ = 26.603° is assigned to the (002) plane of graphitic carbon (PDF#25–0284), revealing that the carbon matrix possesses a partially nanocrystalline graphitic structure rather than a fully amorphous state. Such a microstructure guarantees efficient electron transfer and favorable conductivity, while the broadened peak shape implies a limited microcrystal size[20]. Together with the amorphous domains, this feature contributes to a well-developed porous structure favorable for ion adsorption[21]. Meanwhile, the peak at 2θ = 43.406° is consistent with the (102) plane of FeS (PDF#50-1788), confirming that the optimized precursor ratio triggers a sufficient sulfidation reaction between $FeCl_3$ and MoS_2. As a result, highly crystalline FeS nanocrystals are in-situ anchored on the carbon matrix instead of iron oxides, demonstrating a strong interaction between $FeCl_3$ and MoS_2.In contrast, the diffraction peaks of BPCM-1-1-800 are mainly ascribed to the (012) and (104) planes of Fe_2O_3 (PDF#01-1053), indicating that no effective sulfidation occurs at this precursor ratio. A slight peak shift relative to the standard card is observed for BPCM-1-1-800, which is not caused by instrumental error but is most likely due to the doping of Mo^{6+} (derived from MoS_2) into the Fe_2O_3 lattice at high temperature, thus modifying the lattice parameters[10]. This atomic-level Fe-Mo-O interaction tailors the electronic structure of the material, which may improve conductivity and electrochemical activity, matching well with the pseudocapacitive behavior in the following electrochemical measurements[22]. Additional diffraction peaks at 2θ = 43.472° and 50.673° correspond

to the (111) and (200) planes of iron-based species (PDF#23–0298), verifying the successful introduction of Fe components and their synergistic effect with the carbon framework[23].

Raman spectroscopy (Fig. 3b) was further employed to analyze the graphitization degree of the BPCM-x-y-z series samples. The D band at approximately 1330 cm^{-1} is associated with structural defects and disordered carbon, while the G band at around 1580 cm^{-1} reflects the in-plane stretching vibration of sp^2 hybridized carbon atoms, representing the ordered graphitic structure[24]. The I_D/I_G ratio is widely used as a key indicator to evaluate the graphitization degree, where a lower ratio suggests higher structural order and fewer defects[25]. The I_D/I_G values of BPCM-1-1-800, BPCM-1-2-800, BPCM-1-3-800 and BPCM-1-4-800 were calculated to be 0.88, 0.86, 0.84 and 0.81. Respectively, showing a gradual decline with the increase of KOH/hydrothermal carbon mass ratio. This trend demonstrates that a higher KOH ratio effectively promotes the graphitization process and optimizes the ordering of sp^2 carbon domains. Notably, BPCM-1-2-800 delivered the optimal electrochemical performance even with a moderate I_D/I_G ratio, demonstrating that the capacitive performance of porous carbon is determined by the synergistic regulation of graphitization degree, pore structure, and surface active sites, rather than a single structural parameter[26]. A reduced I_D/I_G ratio enhances the structural order of sp^2 domains and lowers electron transport resistance, which accounts for the higher conductivity of BPCM-1-3-800 and BPCM-1-4-800 compared with BPCM-1-1-800. Nevertheless, excessive graphitization (I_D/I_G ≤ 0.84) may lead to over-etching of the carbon skeleton by KOH, resulting in the collapse of the porous structure, impaired ion diffusion and adsorption, and thus weakening the advantages of high conductivity. In comparison, BPCM-1-2-800 (I_D/I_G = 0.86) achieves a well-balanced graphitization degree, which guarantees fast electron transfer without sacrificing the porous structure caused by over-etching. Its moderate disordered structure preserves abundant defect sites and oxygen-containing functional groups, which supply additional pseudocapacitance and enhance the electrode-electrolyte interaction[27]. For BPCM-1-1-800, the relatively high I_D/I_G ratio (0.88) implies insufficient graphitization, severe structural disorder, poor electron transport efficiency, and undeveloped porosity, leading to poorer electrochemical performance than BPCM-1-2-800.Overall, the I_D/I_G value of BPCM-1-2-800 falls within the optimal range for balancing ordered and disordered structures, enabling the synergistic optimization of electron transport, ion storage, and surface active sites, which is the essential reason for its outstanding electrochemical properties[28].

3.3 The morphological characteristics of BPCM-x

Figure 4 presents the SEM morphologies of $FeCl_3/MoS_2$ co-modified moso bamboo-derived porous carbon samples prepared with different $FeCl_3$ concentrations.BPCM-0.5-2-800 (Fig. 4a) exhibits an irregular and agglomerated morphology, composed of stacked thin plates and blocks with wrinkled surfaces, forming loosely distributed layered pores with relatively poor connectivity.BPCM-1-2-800 (Figs. 4b) obtained at 1.0 M $FeCl_3$ shows a continuous, sponge-like porous framework without obvious bulk aggregation, constructing a three-dimensional interconnected honeycomb network[29]. It features a distinct hierarchical porous structure in which large pores contain abundant small pores. The intertwined thin sheets and irregular blocks create numerous open voids and a highly permeable pore system. This

favorable structure significantly accelerates ion transport: large pores act as rapid transport channels to shorten diffusion paths, while small pores provide abundant active sites for charge storage. Meanwhile, the thin and wrinkled pore walls greatly enlarge the electrode-electrolyte contact area, increasing accessible active sites and decreasing charge-transfer impedance[30]. BPCM-1.5-2-800 (Fig. 4c) displays a compact and homogeneous porous aggregate structure assembled by densely packed tiny, folded units, forming an integrated honeycomb texture dominated by uniform micro/mesopores. This morphology is caused by excessive $FeCl_3$, which induces the collapse of pore walls and the fusion of mesopores, thus reducing the mesopore proportion while generating more micropores. The EDS elemental mapping images (Figs. 4d-4g) verify the homogeneous distribution of C, Fe, Mo, and S throughout the material. Fe appears as discrete fine particles with no significant aggregation (Fig. 4e), whereas Mo exhibits dense and uniform signals covering the entire sample (Fig. 4f). Such a Mo-dominated matrix with highly dispersed Fe species directly confirms the successful synergistic modification of $FeCl_3$ and MoS_2. Compared with previous reports, this work systematically reveals the formation mechanism of highly efficient conductive networks and densely distributed active sites, clarifies the multi-scale structural regulation principles for charge transfer and interfacial interaction, and achieves the simultaneous improvement of specific capacitance and cycling stability. It provides a novel and effective strategy for preparing high-performance biomass carbon electrodes and offers new perspectives and experimental foundations for the design of next-generation, low-cost and sustainable supercapacitor electrode materials.

3.4 Chemical property characterization of BPCM-x

X-ray photoelectron spectroscopy was utilized to analyze the surface chemical composition and elemental valence states of the as-prepared porous carbon materials. All spectra were calibrated using the C 1s peak at 284.80 eV before peak fitting. The full survey spectrum of BPCM-1-2-800 (Fig. 5a) reveals the presence of dominant C, Fe, Mo, and S elements, confirming the successful co-modification of $FeCl_3$ and MoS_2.The high-resolution C 1s spectrum (Fig. 5b) can be fitted into four component peaks, corresponding to C-C (284.80 eV), C-O (285.64 eV), C = O (286.41 eV), and COO^- (289.65 eV). The sp^2 carbon content is significantly higher than that of sp^3 carbon bonded with oxygen-containing groups, indicating a well-preserved graphitic structure. The O 1s spectrum (Fig. 5c) is deconvoluted into C-O (531.30 eV), C = O (533.24 eV), COO^- (535.10 eV), and Mo-O (530.74 eV) bonds. The abundant oxygen-containing functional groups improve the surface wettability of electrode and promote ion diffusion into the internal pore channels. The Mo 3d spectrum (Fig. 5d) is fitted into four peaks: Mo^{2+} (228.74 eV, Mo 3d5/2), which may originate from Mo-C bonds, Mo^{4+} (232.42 eV), and Mo^{6+} (233.07 eV and 236.10 eV). The high-valence Mo^{6+} species are generated by the Fe-induced redox reaction of Mo^{4+}, which effectively enhances the pseudocapacitive performance[31]. The high-resolution S 2p spectrum (Fig. 5e) was deconvoluted into four components. The dominant doublet at 163.95 eV (S 2p3/2) and 165.25 eV (S 2p1/2) are assigned to S^{2-} in MoS_2, confirming deconvolutedng of MoS_2 on the carbon matrix. The peak at 168.65 eV corresponds to high-valence sulfate (SO_4^{2-}), and the peak at 170.75 eV is ascribed to partially oxidized sulfoxide (S = O)[32]. These oxidized sulfur species originate from the redox reactions

induced by Fe^{3+} during the synergistic modification, providing additional electroactive sites for pseudocapacitance.

3.5 Electrochemical Performance

To explore the effect of activation temperature on the electrochemical behavior of bamboo-derived porous carbon, systematic electrochemical characterizations were conducted on a series of BPCM-x-y-z samples. Figure 6a presents the CV curves of BPCM-1-2-800 at scan rates ranging from 5 to 100 mV s^{-1}. Even at a high scan rate of 100 mV s^{-1}, the curve maintains a nearly rectangular shape with excellent symmetry, demonstrating typical ideal EDLC characteristics, which can be attributed to its unique ordered mesoporous network. A pair of obvious redox peaks appears at approximately − 0.6 V and − 0.8 V when the scan rate is 10 mV s^{-1}, revealing remarkable pseudocapacitive behavior. Such pseudocapacitance mainly stems from three aspects: oxygen-containing functional groups on the carbon skeleton, the Fe^{2+}/Fe^{3+} redox reaction of Fe-based species, and the Mo^{4+}/Mo^{6+} redox reaction[23]. Therefore, the total capacitance of BPCM-1-2-800 is jointly contributed by the EDLC derived from the ultrahigh specific surface area and the pseudocapacitance originating from surface functional groups and metal redox couples[33].

The GCD curves of BPCM-1-2-800 at various current densities (Fig. 6b) maintain regular triangular shapes without obvious distortion even at 20 A g^{-1}, confirming outstanding coulombic efficiency. At 0.5 A g^{-1}, the curve shows a standard isosceles triangle profile with negligible voltage drop, representing ideal capacitive energy storage behavior. A slight voltage platform in the discharge segment from − 0.8 V to -0.4 V corresponds well to the redox peaks in the CV curves, which is a typical pseudocapacitive feature, reflecting rapid and reversible Faradaic reactions that provide extra capacity during the charge-discharge process[34].

The influence of activation temperature on electrochemical performance was further investigated under 700°C, 800°C, and 900°C. CV results (Fig. 6c) indicate that BPCM-1-2-800 exhibits the highest specific capacitance and optimal comprehensive performance, which is closely related to the temperature-dependent regulation of structure and surface properties. Excessively high temperature (900°C) leads to thermal decomposition of surface functional groups, sharply reducing pseudocapacitance and overall electrochemical performance. Relatively low temperature (700°C) restricts the KOH activation effect, resulting in insufficient pore formation, limited pore depth, and disconnected pore channels, which increase ion transport resistance and degrade electrochemical properties[35].

The larger enclosed area of the CV curve for BPCM-1-2-800 arises from its synergistic structural and compositional advantages, including high specific surface area, well-developed mesoporous structure, and abundant surface functional groups and metal active species. Notably, the CV curve of BPCM-1-2-800 still maintains the most ideal quasi-rectangular profile even at 100 mV s^{-1}, confirming superior fast charge-discharge capability. GCD results (Fig. 6d) further verify the optimal performance of BPCM-1-2-800. Based on the above CV and GCD tests, 800°C is determined as the optimal activation temperature.

Systematic characterizations were also carried out to explore the effect of KOH/hydrothermal carbon activation mass ratio on the electrochemical performance of BPCM-x-y-z. All samples display regular rectangular CV curves at 20 mV s^{-1}, reflecting excellent fast charge-discharge ability, and BPCM-1-2-800 shows the largest integral area, indicating superior specific capacitance (Fig. 7a). Correspondingly, the highly symmetrical GCD curves (Fig. 7b) prove superior reaction reversibility, and BPCM-1-2-800 possesses the longest charge-discharge time due to its maximum specific surface area, which is consistent with CV results. The specific capacitance increases from 330 F g^{-1} (mass ratio 1:1) to 450 F g^{-1} (mass ratio 2:1) and decreases significantly beyond the mass ratio of 2:1, confirming that 2:1 is the optimal activation mass ratio.

EIS tests were applied to reveal the mechanism behind performance differences, and the equivalent circuit diagram was fitted by Z-view software (Fig. 8f). EIS curves (Figs. 6e and Figs. 7c) show that all samples exhibit nearly vertical lines in the low-frequency region, representing ideal capacitive behavior. BPCM-1-2-800 possesses the smallest equivalent series resistance (Rs), benefiting from its high specific surface area and hierarchical porous structure that enable rapid charge diffusion, as well as the lowest charge transfer resistance (Rct), owing to the abundant 2–8 nm micro/mesopores that facilitate ion diffusion. In contrast, BPCM-1-2-900 shows a larger Rs value, which may be caused by poor wettability and pore structure deterioration due to low oxygen content.

Figure 8 compares BPCM-2-800 and BPCM-1-2-800. Figure 8a conducted CV tests on BPCM-2-800 and BPCM-1-2-800 at 20 mV s^{-1}. The closed area of BPCM-1-2-800 is significantly larger than that of BPCM-2-800, which intuitively proves that the electrochemical activity and charge storage capacity of the material are significantly enhanced after $FeCl_3$ regulation[36]. The constant current discharge curve in Fig. 8b shows that the BPCM-1-2-800 has a longer discharge time, corresponding to a higher actual specific capacity, further confirming its excellent energy storage performance. EIS (Fig. 8c) demonstrates that BPCM-1-2-800 exhibits an impedance curve closer to the origin, implying significantly reduced charge-transfer resistance and accelerated charge transport dynamics. The specific capacitance data in Fig. 8d more directly presents the efficiency enhancement effect. The specific capacitance of BPCM-2-800 is only 230 F g^{-1}, while after the synergistic modification of FeCl3, the specific capacitance of BPCM-1-2-800 increases to 450 F g^{-1}, which is significantly better than the MoS2/ bamboo carbon system without $FeCl_3$[37]. This provides core support for the capacitance improvement and stability optimization of composite electrode materials.

3.6 Rate Performance and Cycling Stability

Figures 6f and Figs. 7d display the rate performance of BPCM-x-y-z samples at different current densities. Compared with other carbon electrodes, BPCM-1-2-800 still delivers a maximum specific capacitance of 270 F g^{-1} even at 20 A g^{-1} and shows the most gradual capacitance decay as the current density increases from 0.5 A g^{-1} to 20 A g^{-1}. This advantage is attributed to its unique interconnected 3D honeycomb network, in which mesoporous channels shorten ion diffusion paths and ensure stable high-rate performance. Impressively, BPCM-1-2-800 exhibits extraordinary cycling stability

(Fig. 8e). After 5000 charge-discharge cycles at 10 A g^{-1}, the capacitance retention rate remains as high as 95%. Such outstanding stability originates from multiple synergistic mechanisms: the graphitic carbon framework after high-temperature activation provides robust mechanical support; uniformly dispersed MoS_2 nanosheets ensure continuous electron transport; appropriate Fe doping induces the Mo^{4+}/Mo^{6+} redox reaction to enhance pseudocapacitance without damaging structural integrity. These synergistic effects optimize the charge storage mechanism of BPCM-1-2-800, endowing it with promising capacitive performance. This work systematically clarifies the construction principle of efficient conductive networks and dense active sites, reveals multi-scale structural regulation rules for charge transport and interface response, and achieves synchronous improvement of capacitance and cycling stability. It provides a novel strategy for preparing high-performance biomass carbon electrodes and offers new insights and experimental foundations for the design of next-generation high-performance, low-cost, and sustainable supercapacitor electrode materials. Three complementary characterization methods mutually verify and form a closed-loop analysis, providing solid support for the excellent electrochemical performance of BPCM-1-2-800. CV tests reveal the synergistic energy storage mechanism of EDLC and pseudocapacitance and the regular quasi-rectangular profile and typical redox peaks confirm the efficient coupling of the two energy storage modes. EIS results verify the optimized interfacial charge transfer properties of the material, with minimal charge transfer resistance and near-ideal capacitive impedance response, indicating high charge transport efficiency. GCD measurements directly demonstrate superior cycling stability, with 95% capacitance retention after 5000 cycles at 10 A g^{-1}, highlighting reliable structure and performance. As listed in Table 2, BPCM-1-2-800 outperforms most reported biomass-derived carbon and modified electrodes, with comparable or even superior cycling stability, reflecting strong comprehensive advantages. Such excellent performance stems from the Fe-MoS_2 synergistic effect (Fe-based active sites, optimized MoS_2 phase and defects) and hierarchical porous structure, whose combination simultaneously enhances capacitance and stability.

Table 1
Pore Structure Parameters of BPCM-x-y-z

sample	SBET ($cm^2\ g^{-1}$)	Smic ($cm^2\ g^{-1}$)	Smeso ($cm^2\ g^{-1}$)	Vtotal ($cm^3\ g^{-1}$)	Vmic ($cm^3\ g^{-1}$)	Vmeso ($cm^3\ g^{-1}$)
BPCM-0.5-2-800	1200.78	546.35	654.43	0.542	0.115	0.427
BPCM-1-2-800	2164.37	1785.61	378.76	0.951	0.375	0.576
BPCM-1.5-2-800	1731.45	1424.98	306.47	0.742	0.297	0.445
BPCM-1-2-700	1127.82	364.62	763.20	0.563	0.147	0.416
BPCM-1-2-900	1932.43	1614.46	317.97	0.825	0.336	0.489

Table 2
A comparison of the values of specific capacitance in this study with other studies reported in the literature.

Electrodes	Electrolyte	Specific capacitance (F g^{-1})	Conditions	Ref.
MoS_2/Mo	1 M Na_2SO_4	192.7	1mA cm^{-2}	11
MoS_2-16	1 M Na_2SO_4	518.7	1 A g^{-1}	12
a-CSHs	6M KOH	238	0.5 A g^{-1}	29
CLHPC-2	1M H_2SO_4	230	0.1 A g^{-1}	30
BPCM-1-2-800	6M KOH	450	0.5 A g^{-1}	This work

3.7 Electrochemical performance of symmetric two-electrode supercapacitor

To further evaluate the practical application potential of optimized BPCM-1-2-800 electrode material, symmetric two-electrode supercapacitors were assembled using identical BPCM-1-2-800 electrodes and 6 M KOH aqueous electrolyte. The electrode fabrication procedure was consistent with the three-electrode system, and the device tests were carried out within a voltage window of 0–1.0 V.

Figure 9a presents CV curves of the symmetric device at scan rates ranging from 5 to 100 mV s^{-1}. All curves retain quasi-rectangular profiles without obvious polarization distortion, demonstrating the coexistence of dominant electric double-layer capacitance and weak pseudocapacitive redox humps at 0.45–0.65 V, which correspond to the reversible Fe^{2+}/Fe^{3+} and Mo^{4+}/Mo^{6+} Faradaic reactions. Even at a high scan rate of 100 mV s^{-1}, the CV shape remains intact, revealing outstanding ion diffusion kinetics enabled by the interconnected hierarchical micro-mesoporous network of BPCM-1-2-800.The GCD profiles recorded at current densities of 0.5–20 A g^{-1} are displayed in Fig. 9b. All charge-discharge curves exhibit highly symmetric triangular shapes with negligible IR drop. At 0.5 A g^{-1}, the symmetric device delivers a prominent device capacitance of 242 F g^{-1}. When the current density rises to 20 A g^{-1}, the device still maintains 146 F g^{-1}, corresponding to a capacitance retention of 60.3%, which confirms excellent rate capability. The mild voltage plateau in the discharge segment further verifies the pseudocapacitive contribution from metal redox couples and oxygen-containing functional groups.

The Ragone plot (Fig. 9c) summarizes the energy-power density characteristics of the device. The assembled symmetric supercapacitor achieves a maximum energy density of 28.6 Wh kg^{-1} at a power density of 250 W kg^{-1}. Even under an ultrahigh power density of 10000 W kg^{-1}, the device still retains an energy density of 16.3 Wh kg^{-1}, which is superior to most reported biomass carbon-based symmetric devices under identical alkaline electrolyte conditions.

Long-term cycling stability of the symmetric device was tested at 10 A g^{-1} for 10000 continuous charge-discharge cycles (Fig. 9d). The device retains 92.3% of its initial capacitance after cycling. The slight capacity decay originates from minor electrolyte consumption and mild structural expansion during repeated ion intercalation/deintercalation, while the robust carbon skeleton anchored with homogenously distributed MoS_2 and Fe-based nanoparticles effectively inhibits pore collapse and material exfoliation, guaranteeing reliable long-cycle performance for practical supercapacitor applications.

Overall, the outstanding electrochemical performance of the BPCM-1-2-800 symmetric device further validates the synergistic enhancement effect of $FeCl_3$-MoS_2 co-modification on bamboo-derived porous carbon, demonstrating great application prospects for low-cost, green biomass-based energy storage electrodes.

3.8 Formation Mechanism of $FeCl_3$-MoS_2 Synergistically Modified Bamboo-Derived Porous Carbon

To further clarify the construction process and formation mechanism of the material, Fig. 10 schematically illustrates the synthesis pathway and structural evolution of $FeCl_3$-MoS_2 synergistically modified bamboo powder-based porous carbon. The formation of $FeCl_3$-MoS_2 co-modified bamboo porous carbon relies on hydrothermal coupling, $FeCl_3$-mediated pore-defect regulation, and high-temperature activation reconstruction. During hydrothermal treatment, bamboo powder is preliminarily carbonized to form a porous carbon skeleton with abundant oxygen-containing groups, which anchor MoS_2 nanosheets and Fe^{3+} ions. Fe^{3+} induces partial carbon etching to generate initial micro-mesopores, while triggering defect engineering in MoS_2 to create S vacancies and edge defects, improving conductivity and exposing active sites. Subsequent KOH activation at 800°C further etches the carbon framework, constructing a 3D hierarchical micro-mesoporous network with ultrahigh specific surface area. Meanwhile, Fe^{3+} is partially reduced and reacts with S from MoS_2 to form FeS nanocrystals, enhancing interfacial interaction and inhibiting MoS_2 agglomeration. The synergistic effect optimizes pore structure, regulates defects, and enriches active sites, endowing BPCM-1-2-800 with superior electrochemical performance.

4 Conclusions

In this work, a hydrothermal-assisted $FeCl_3$-MoS_2 synergistic strategy was developed to prepare bamboo powder-derived porous carbon for high-performance supercapacitors, with emphasis on its pseudocapacitive behavior and high-efficiency energy storage mechanism. $FeCl_3$ acts as a multifunctional regulator to construct hierarchical micro/mesoporous networks, induce defect engineering in MoS_2 and provide abundant Fe-based redox sites. The optimized BPCM-1-2-800 exhibits a large specific surface area of 2164.37 m^2g^{-1}, a high specific capacitance of 450 F g^{-1} at 0.5 A g^{-1}, and 95% capacitance retention after 5000 cycles at 10 A g^{-1} in 6 M KOH electrolyte. The pseudocapacitive

response arises from reversible redox reactions of Mo^{4+}/Mo^{6+}, Fe^{2+}/Fe^{3+} and oxygen-containing functional groups, which deliver extra faradaic capacitance besides the electric double-layer contribution. Efficient energy storage originates from the synergistic coupling of a hierarchical porous structure. This work verifies that $FeCl_3$-MoS_2 synergistic modification effectively enhances pseudocapacitive activity and efficient energy storage performance of biomass carbon. The green, low-cost and scalable route, coupled with the clarified mechanism, provides a promising strategy for designing advanced biomass-based electrodes with outstanding pseudocapacitive.Moreover, the symmetric two-electrode supercapacitor assembled with BPCM-1-2-800 delivers a high device capacitance of 242 F g^{-1} at 0.5 A g^{-1}, a maximum energy density of 28.6 Wh kg^{-1} and 92.3% capacitance retention after 10000 cycles, further demonstrating its great practical value for advanced supercapacitor devices.

Declarations

Declaration of competing interest

The authors declare that they have no known competing financial interests or personal relationships that could have appeared to influence the work reported in this paper.

Author Contribution

C. conceived the research framework. L. performed the whole experiments and wrote the main-text manuscript. B. and S. analyzed experimental data. W. and Z. took part in partial experimental operations. Q. and L. carried out data sorting and collation. All authors reviewed the manuscript.

Acknowledgment

We gratefully acknowledge the financial support provided by the National Key R&D Program of China (Grand No.2024YFC3810200). The research collaboration among the groups and universities of the authors is also gratefully acknowledged.

References

1. Imasiku K, Farirai F, Olwoch J, Agbo SN (2021) Policy Rev Green Hydrogen Econ South Afr vol 13(23):13240
2. Wang H, Zhou P, Zhao X (2025) Applications of Biochar in Fuel and Feedstock Substitution: A Review, vol. 18, no. 17, p. 4511
3. Bi Z et al (2019) Biomass-derived porous carbon materials with different dimensions for supercapacitor electrodes: a review, vol. 7, no. 27, pp. 16028–16045

4. Kumar Y, Rawal S, Joshi B (2019) and S. J. J. o. S. S. E. Hashmi, Background, fundamental understanding and progress in electrochemical capacitors, vol. 23, no. 3, pp. 667–692
5. Zhang Y, Cai Y, Li T, Wang M, Chen X, Xu Y (2024) Synthesis and electrochemical performance of biomass-derived porous carbon materials for supercapacitors %J. J Mater Science: Mater Electron vol 35:1–12
6. Dagwar PP et al (2026) Agricultural waste-derived carbon electrodes for sustainable lithium-ion batteries: environmental and economic assessment. Environ Science: Adv
7. Ali M et al (2022) 2D-TMDs based electrode material for supercapacitor applications. 46(15):22336–22364
8. Chinnappan N, Punniyakoti S (2024) Emerging advances of 2D molybdenum disulfide (MoS2) and their composites towards high-performance supercapacitors: A comprehensive review, *Journal of Energy Storage*, vol. 102, p. 114040, /11/15/ 2024
9. Hanifehpour Y et al (2022) Investigation of the supercapacitor behavior of MoS2and Fe-doped MoS2nano-flowers synthesized using the hydrothermal method. New J Chem 46(43):20932–20939
10. Pan H, Meng X, Qi X, Qin GJC (2017) Electronic and optical properties of MoS 2/α-Fe 2 O 3 (0001) heterostructures: A first-principles investigation. 19(42):6333–6338
11. Krishnamoorthy K, Veerasubramani GK, Pazhamalai P, Kim SJ Designing two dimensional nanoarchitectured MoS2 sheets grown on Mo foil as a binder free electrode for supercapacitors. Electrochim Acta, 190, pp. 305–312, 2016/02/01/ 2016.
12. Wang F, Li G, Zheng J, Ma J, Yang C, Wang Q (2018) Hydrothermal synthesis of flower-like molybdenum disulfide microspheres and their application in electrochemical supercapacitors. RSC Adv 8(68):38945–38954. 10.1039/C8RA04350G
13. Toyoda M, Ohkuma S (2022) Preparation of Porous Carbon from SB-HPC (Sub-Bitumious) Solution Derived from Low Quality Coal and Its Application to EDLC, in *Electrochemical Society Meeting Abstracts 241*, no. 1, pp. 12–12: The Electrochemical Society, Inc
14. Luo L et al (2023) Enhanced capacitance of phosphorus, nitrogen, and oxygen tri-doped balsa wood-based porous carbon for supercapacitors. 58:106339
15. Qiu G et al (2022) Hierarchical porous carbon derived from recycled bamboo waste as supercapacitors electrodes based on FeCl 3 -catalyzed hydrothermal pretreatment: Pore regulation and high-performance analysis. Int J Energy Res 46(15):22971–22990
16. Chen Q, Yuan Y, Yin S, Zhu M, Cai GJN (2020) Pomegranate-like C@ TiO2 mesoporous honeycomb spheres for high performance lithium ion batteries. 31(43):435410
17. Li G et al (2017) Structure and Electrochemical Properties of Pyrolyzed Magnesium Citrate/SU-8 Nanocomposites for Supercapacitators, in *Electrochemical Society Meeting Abstracts 232*, no. 6, pp. 588–588: The Electrochemical Society, Inc
18. Rastogi AC, Sidhu NK Vertically Aligned ZnO/MnO2/Pedot Core-Shell Electrode in 3-D Nano-Architecture for High Energy-Power Density Pseudocapacitive Electrochemical Energy Storage, *ECS Meeting Abstracts*, vol. MA2020-02, no. 3, p. 551, 2020/11/23 2020

19. Wang S, Xiang C, Zou Y, Yang Z, Sun L, Kraatz H-B (2026) Regulation of Oxygen Vacancies in High Entropy Oxides With Multi-Layer Eggshell Architectural Framework for Boosting the Electrochemical Performance of Supercapacitors. 9(3):e70230
20. Wang Y et al (2021) Ball milling-assisted synthesis and electrochemical performance of porous carbon with controlled morphology and graphitization degree for supercapacitors, *Journal of Energy Storage*, vol. 38, p. 102496, /06/01/ 2021
21. Zhao R et al (2026) Dual modulation of pore architecture and surface chemistry in P, N co-doped carbons for high-performance potassium ion hybrid capacitors, *Journal of Energy Storage*, vol. 152, p. 120793, /03/30/ 2026
22. Wu S et al (2024) Phase modulation and electrochemical behavior of Fe3Mo3C/Mo2C composite nanofibers as supercapacitor negative electrodes. 7(21):9827–9838
23. Xu Q-Q et al (2022) Fe-doping induced surface Fe2+/Fe3 + cycle and activated redox-inert TiO2 for enhanced Hg (II) electrochemical sensing: An efficient strategy to strengthen the redox activity. 1232:340472
24. Fasakin O et al (2018) Synthesis and characterization of porous carbon derived from activated banana peels with hierarchical porosity for improved electrochemical performance. 262:187–196
25. Kavrar-Ürk D et al Growth and characterization of carbon nanotubes on FeSi substrates via chemical vapor deposition: influence of synthesis parameters and magnetic properties. J Mater Sci: Mater Electron, 37, 10, p. 775, 2026/04/10 2026.
26. Fan Q, Song C, Fu P (2024) Advances in the improvement of the quality and efficiency of biomass-derived porous carbon: A comprehensive review on synthesis strategies and heteroatom doping effects, *Journal of Cleaner Production*, vol. 452, p. 142169, /05/01/ 2024
27. Zheng Y, Lian Y, Guo H, Zhao J, Zhang H (2023) Enhanced capacitive performance by synergistic effect of interfacial functional groups and doping defects in honeycomb-like multi-chamber carbon, *Applied Surface Science*, vol. 637, p. 157995, /11/15/ 2023
28. Liu Y et al (2025) A partially disordered crystallographic shear block structure as fast-charging negative electrode material for lithium-ion batteries. 16(1):6507
29. Chen H, Wang G, Chen L, Dai B, Yu FJN (2018) Three-dimensional honeycomb-like porous carbon with both interconnected hierarchical porosity and nitrogen self-doping from cotton seed husk for supercapacitor electrode. 8(6):412
30. Yang X, Li C, o. YJJ, Chen PDAP (2017) Hierarchical porous carbon with ultrahigh surface area from corn leaf for high-performance supercapacitors application. 50(5):055501
31. Charapale MR et al (2024) Enhancing capacitive performance of MoS2 through Fe doping: Synthesis, characterization, and electrochemical evaluation for supercapacitor applications, vol. 52, p. 104814
32. Qi K, Yuan Z, Hou Y, Zhao R, Zhang B (2019) Facile synthesis and improved Li-storage performance of Fe-doped MoS2/reduced graphene oxide as anode materials. Appl Surf Sci 483:688–695

33. Qu C et al Functionalized Bimetallic Hydroxides Derived from Metal–Organic Frameworks for High-Performance Hybrid Supercapacitor with Exceptional Cycling Stability. ACS Energy Lett, 2, 6, pp. 1263–1269, 2017/06/09 2017.
34. Liu J et al (2023) Tracking surface ionic movement of Ni3S2@ CuS electrode materials with high electrochemical performance, vol. 461, p. 141910
35. Pinij P, Tippayawong N, Chimupala Y, o. SJJ, Chaiklangmuang A, Pyrolysis A (2021) Performances of functional groups and KOH-transformation in corn stover waste through catalytic pyrolysis. 157:105234
36. Zheng Y, Chen K, Jiang K, Zhang F, Zhu G, Xu H (2022) Progress of synthetic strategies and properties of heteroatoms-doped (N, P, S, O) carbon materials for supercapacitors, *Journal of Energy Storage*, vol. 56, p. 105995, /12/10/ 2022
37. Qiu S et al Using FeCl3 as a Solvent, Template, and Activator To Prepare B, N Co-Doping Porous Carbon with Excellent Supercapacitance, *ACS Sustainable Chemistry & Engineering*, vol. 7, no. 19, pp. 15983–15994, 2019/10/07 2019

Figures

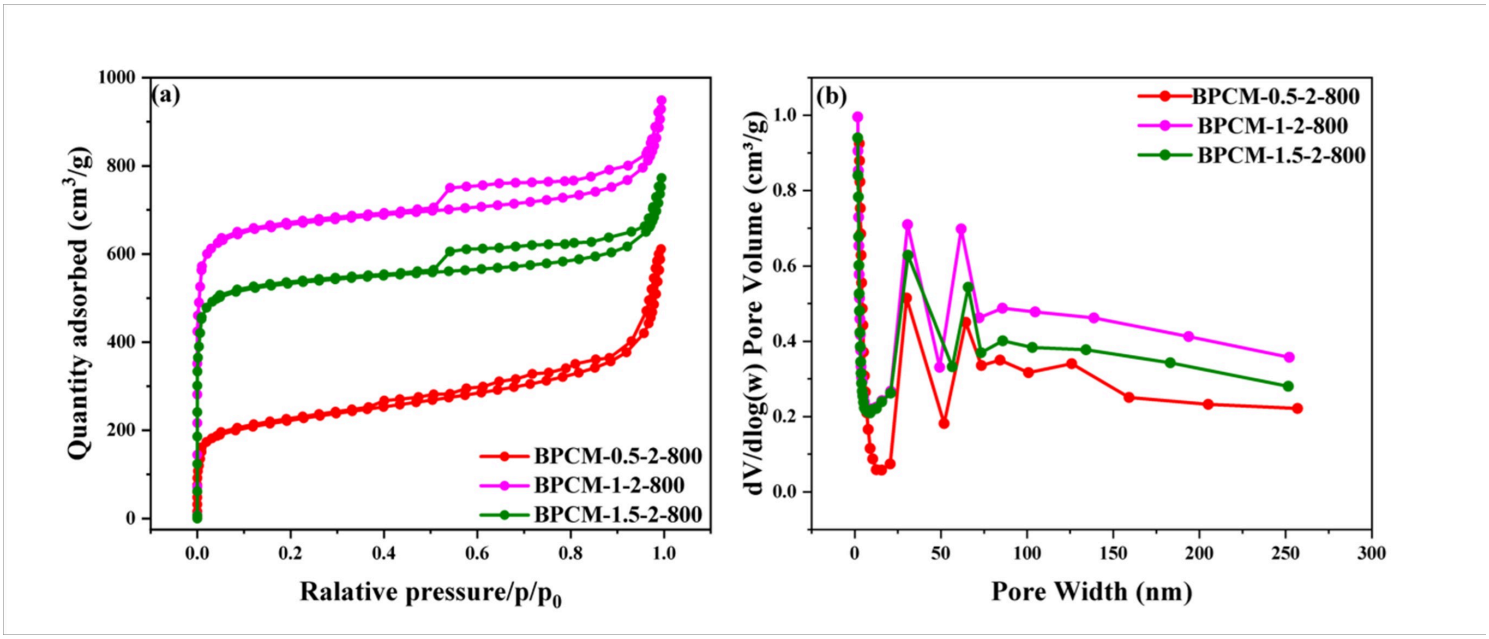

Figure 1

(a) N_2 adsorption/desorption isotherms of BPCM-0.5-2-800, BPCM-1-2-800 and BPCM-1.5-2-800 samples. (b) DFT aperture distribution curves of BPCM-0.5-2-800, BPCM-1-2-800 and BPCM-1.5-2-800.

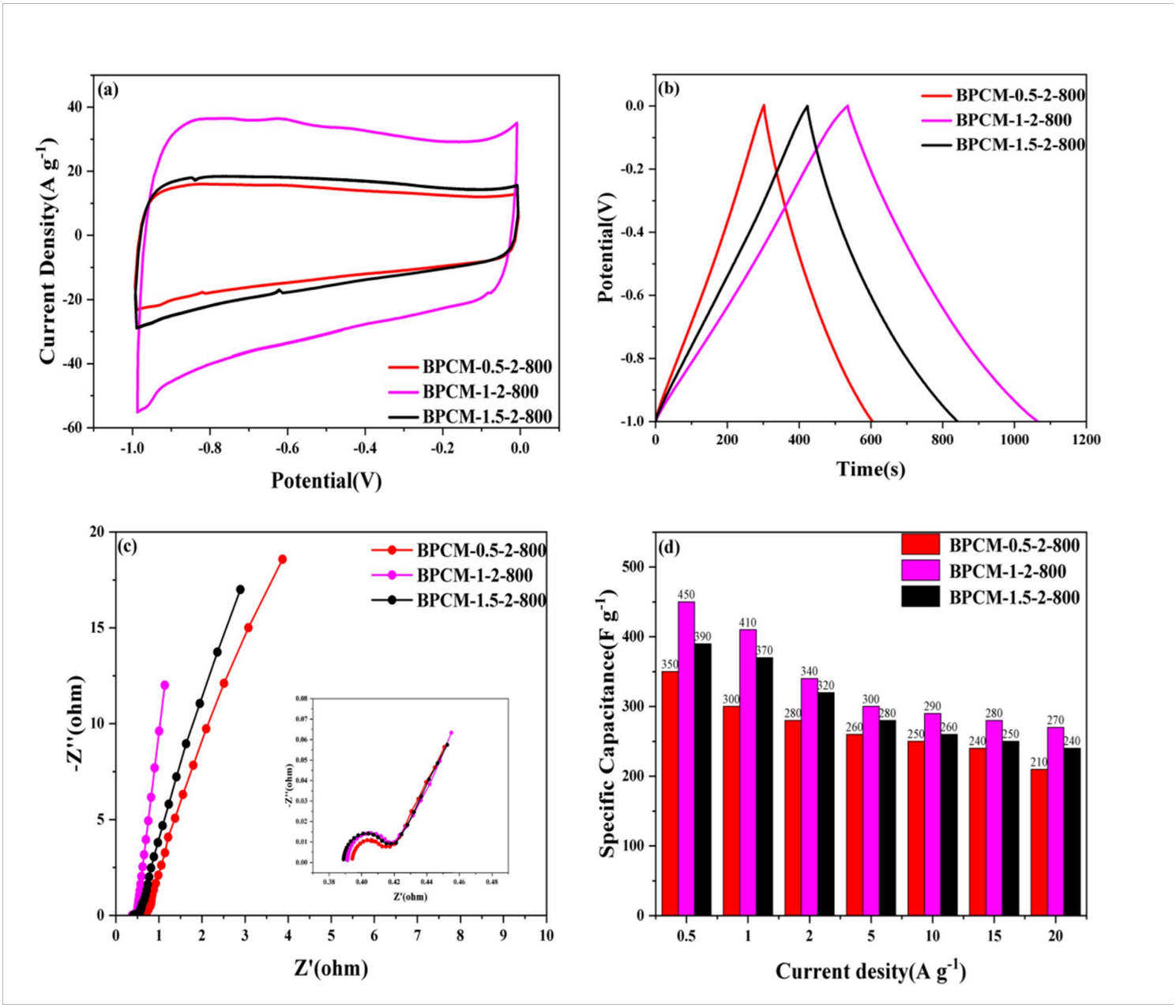

Figure 2

(a) CV curve at 20 mV s^{-1}; (b) GCD curve at 0.5 A g^{-1}; (c) Nyquist plot; (d) Cs curves of BPCM-0.5-2-800, BPCM-1-2-800, and BPCM-1.5-2-800 at different current densities (three-electrode test).

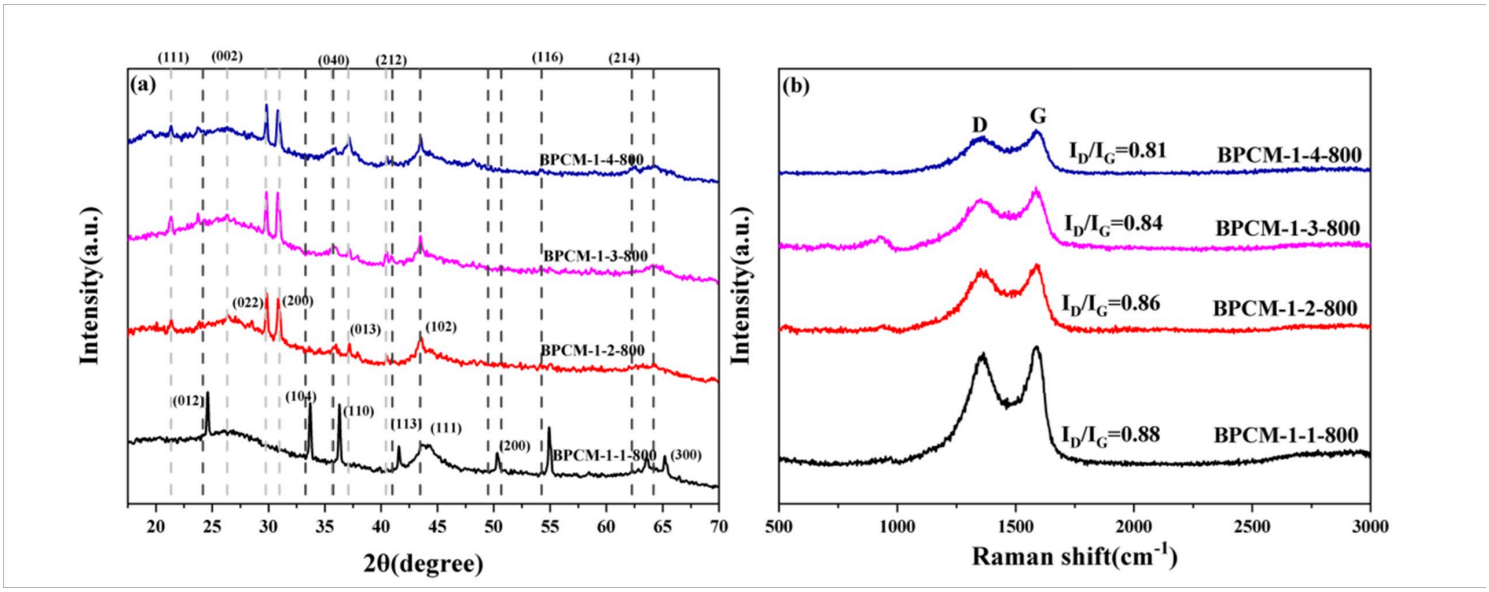

Figure 3

(a) XRD spectra, (b) Raman spectra of BPCM-1-1-800, BPCM-1-2-800, BPCM-1-3-800, and BPCM-1-4-800.

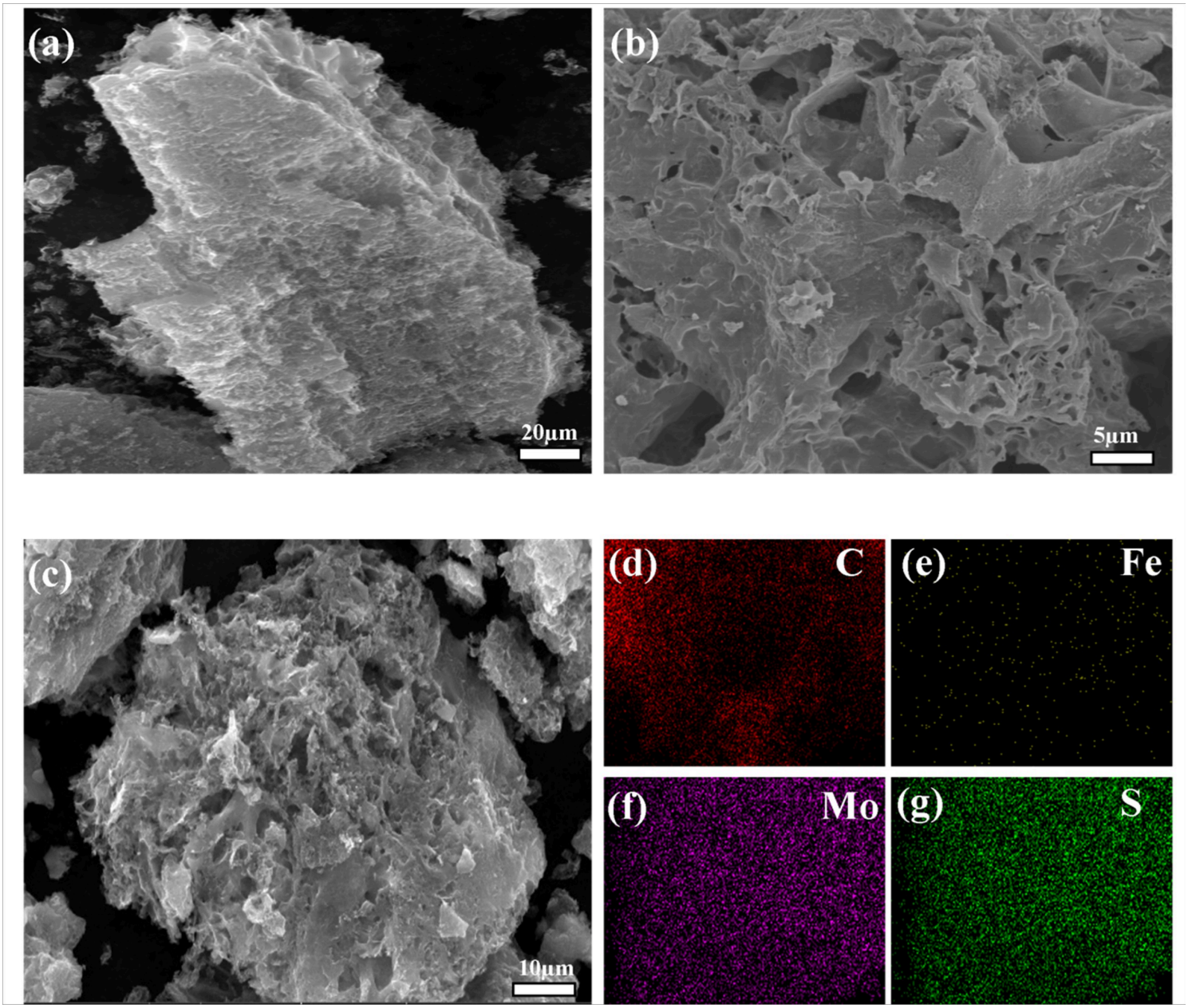

Figure 4

SEM image of BPCM (a)BPCM-0.5-2-800; (b)BPCM-1-2-800; (c) BPCM-1.5-2-800; (d-g) is the EDS diagram of BPCM-1-2-800, in the order of C, Fe, Mo and S.

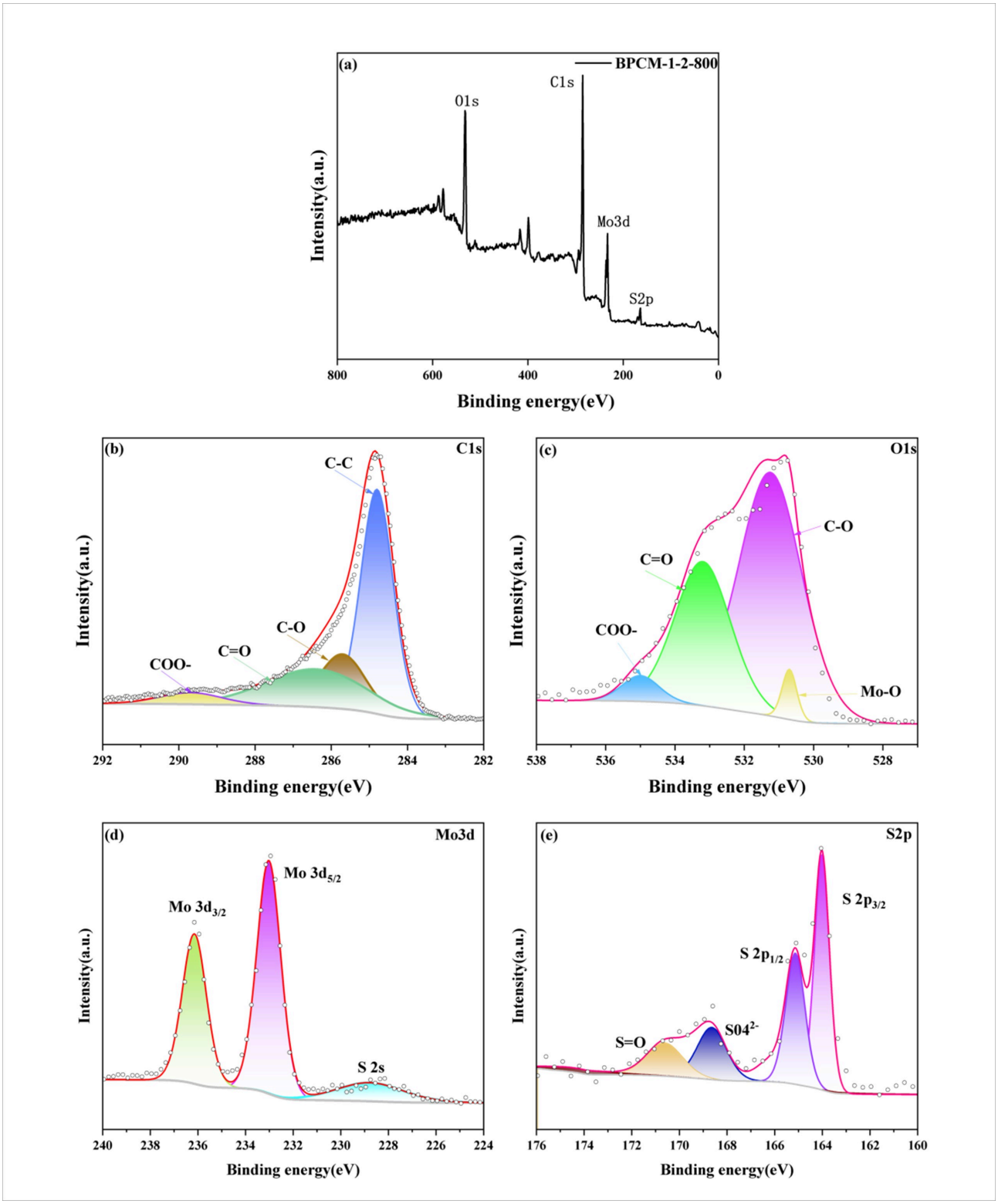

Figure 5

XPS spectra of sample BPCM-1-2-800: (a) total spectrum, (b)C1s, (c)O1s, (d)Mo3d and (e)S2p.

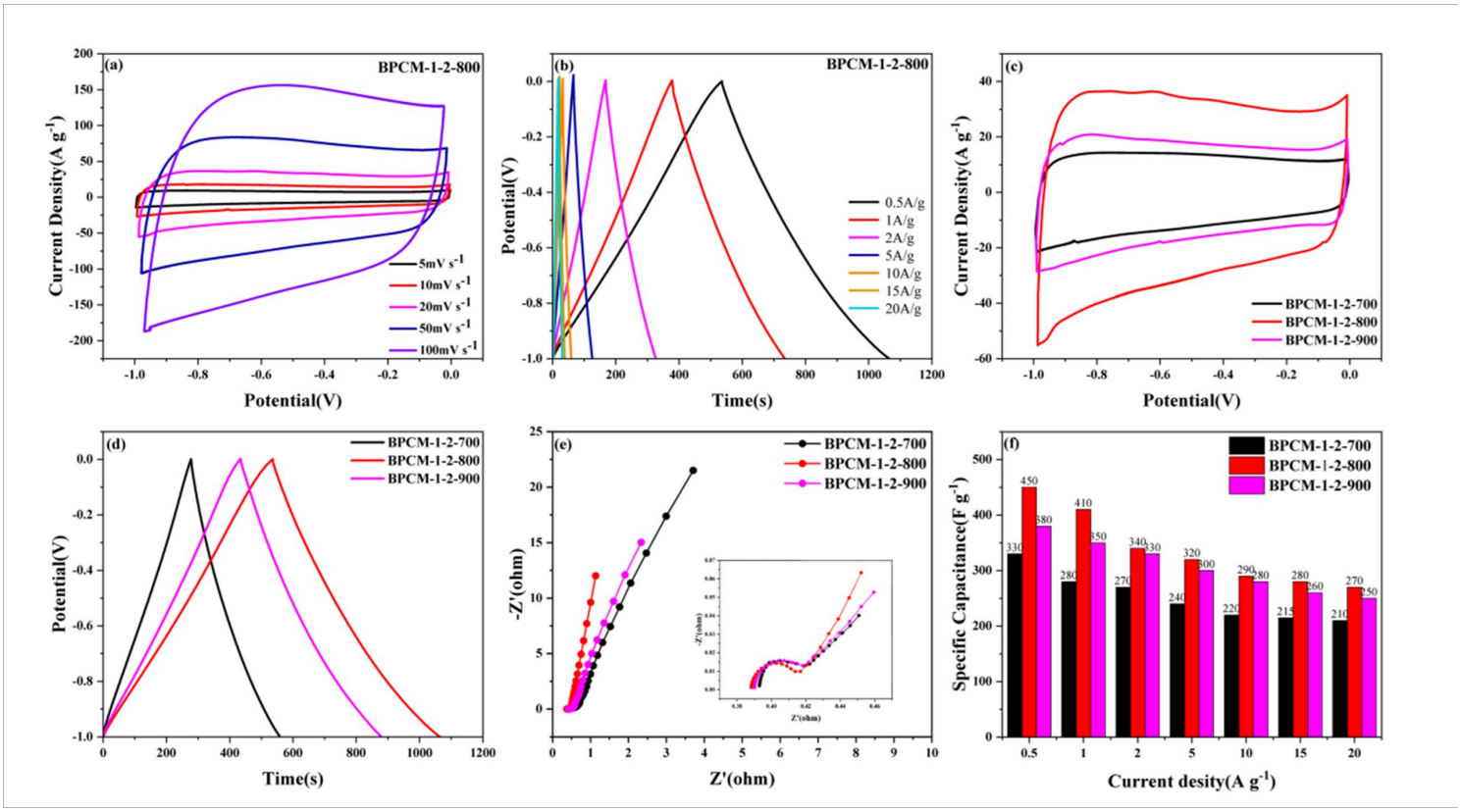

Figure 6

(a) CV curves of BPCM-1-2-800 at various scanning rates; (b) GCD curves of BPCM-1-2-800 at different current densities; (c) CV curves at 20 mV s^{-1}; (d) GCD curves at 0.5 A g^{-1}; (e) Nyquist plots of BPCM prepared at different activation temperatures and potassium hydroxide/hydrothermal carbon ratios;(f)Cs curves.

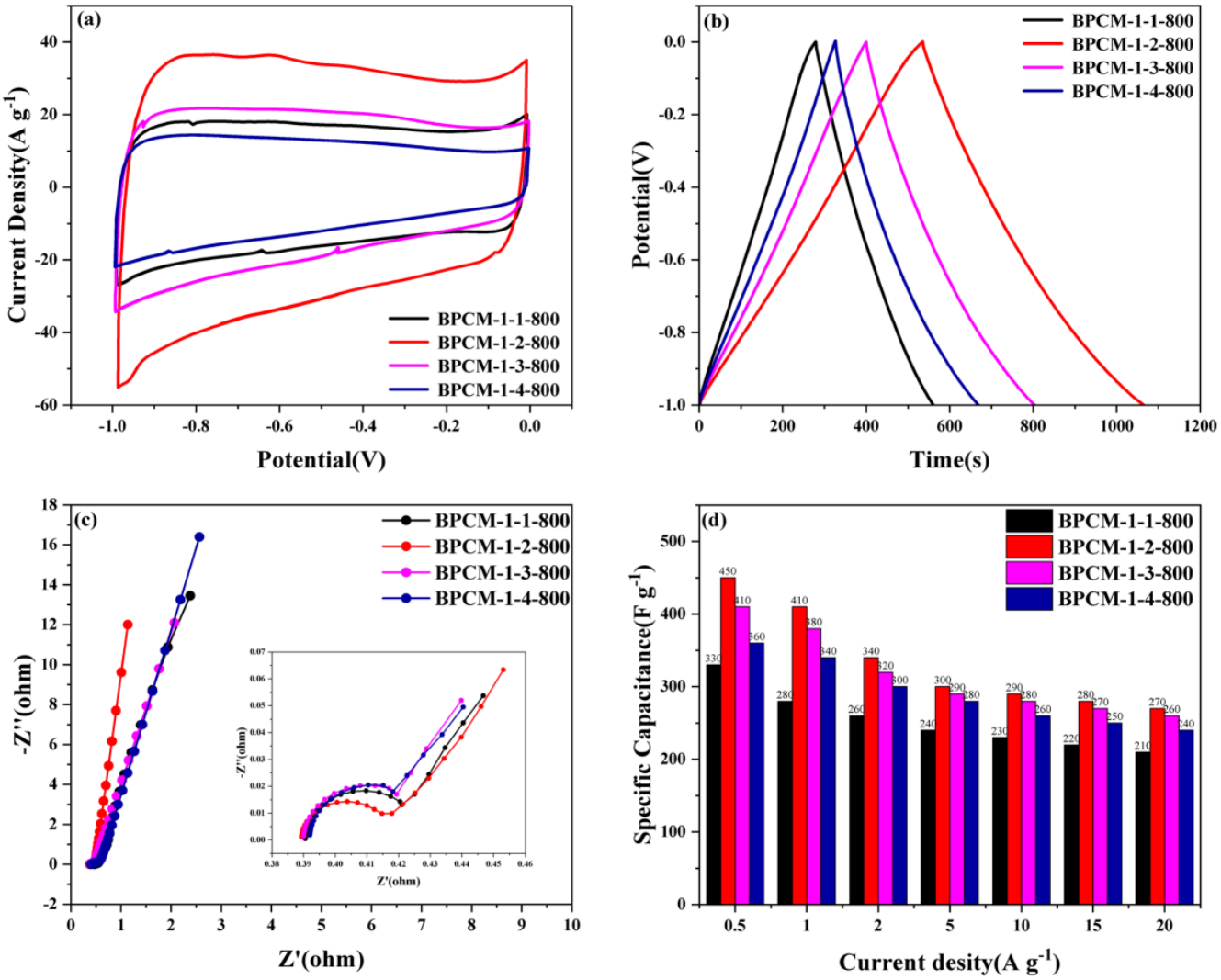

Figure 7

(a) CV curve at 20 mV s^{-1}; (b) GCD curve at 0.5A g^{-1}; (c) Nyquist plot; (d) Cs curves.

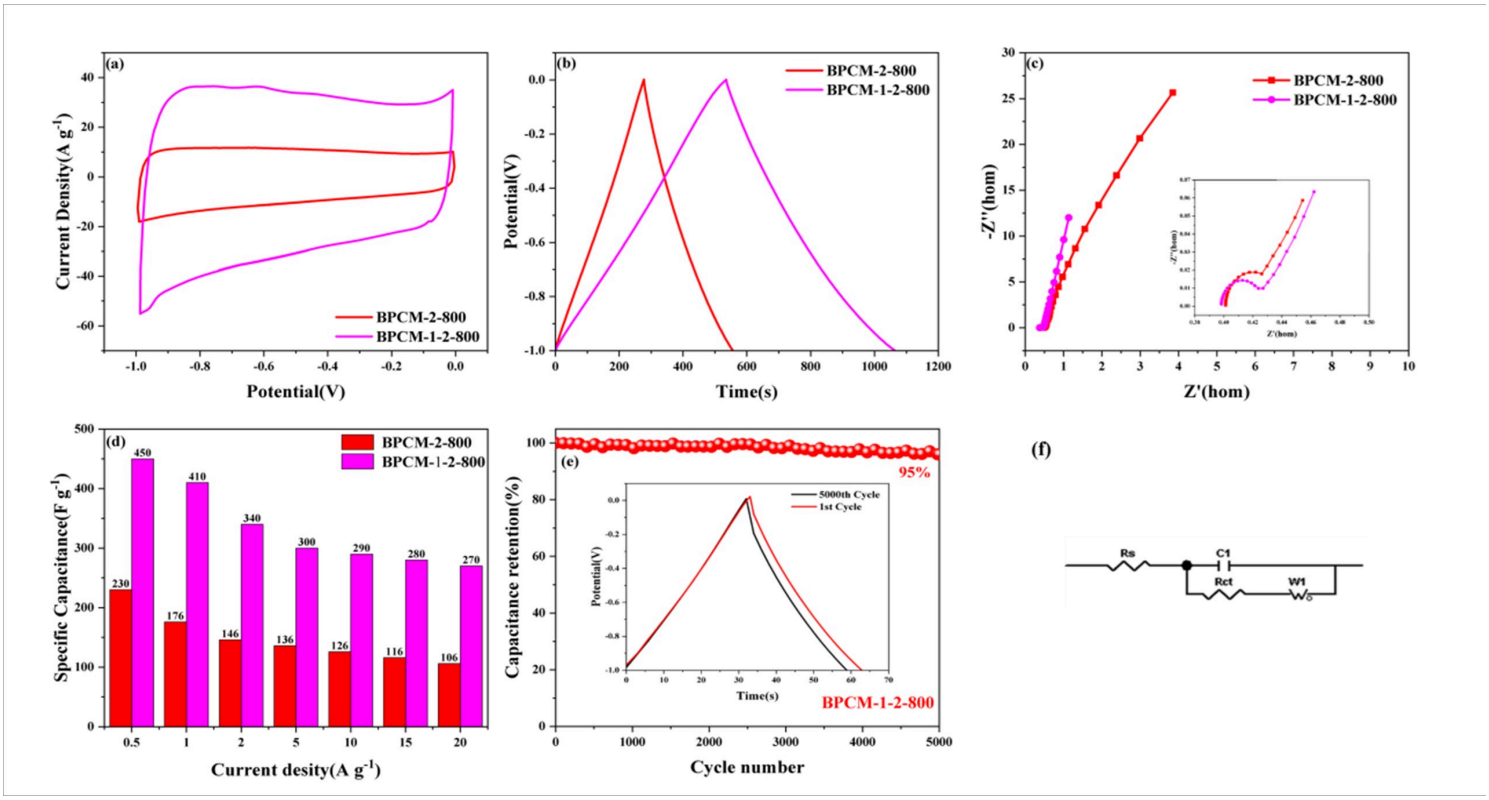

Figure 8

(a) CV curve at 20 mV s^{-1}; (b) GCD curve at 0.5A g^{-1}; (c) Nyquist plot; (d) Cs curves of BPCM-2-800 and BPCM-1-2-800 at different current densities; (e) Stability test of supercapacitors based on BPCM-1-2-800 for 5000 Cycles at 10A g^{-1} current density; (f) corresponding equivalent circuits.

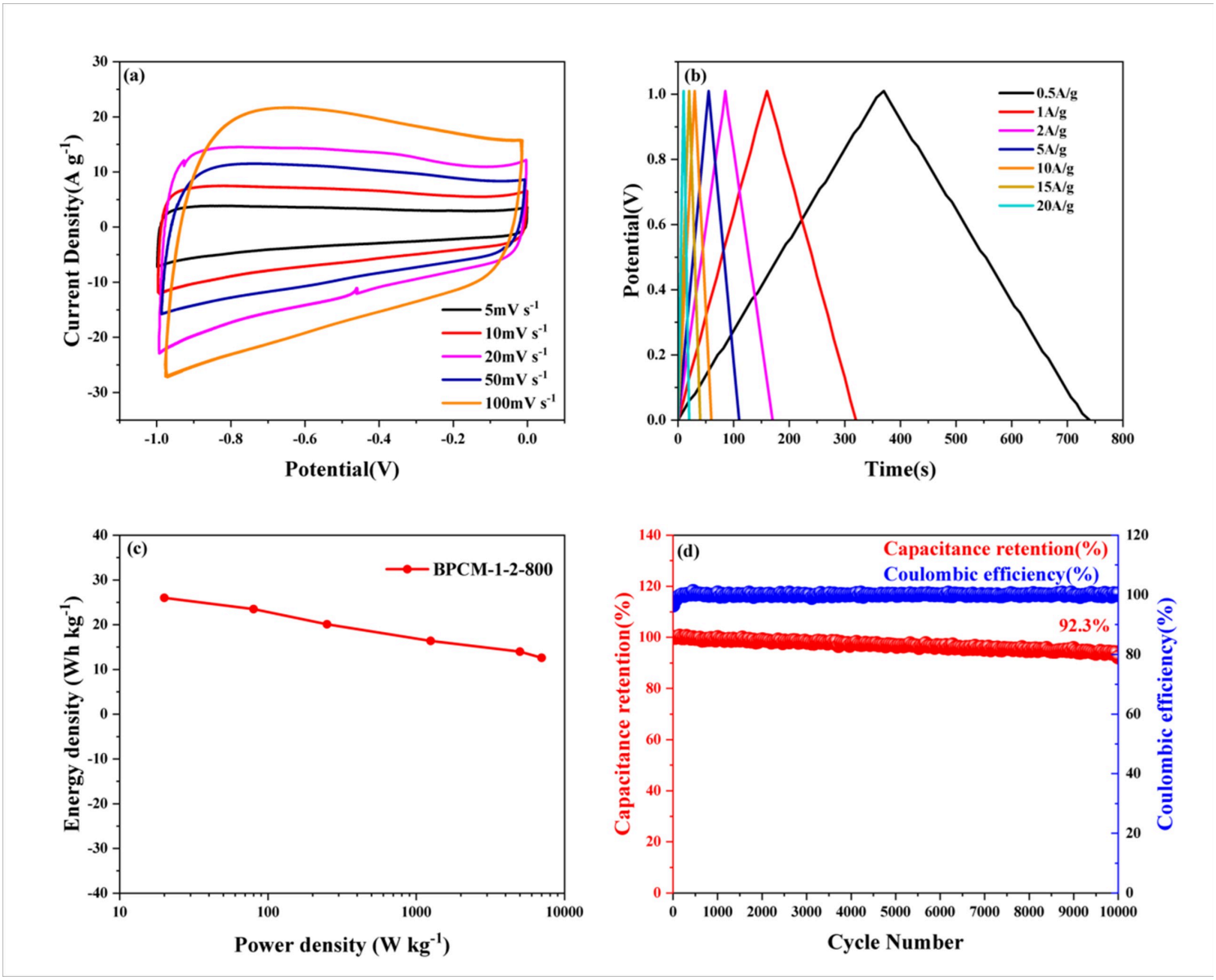

Figure 9

Electrochemical performance of BPCM-1-2-800 symmetric two-electrode supercapacitor in 6 M KOH electrolyte: (a) CV curves at scan rates of 5–100 mV s^{-1} (0–1.0 V); (b) GCD curves at current densities of 0.5–20 A g^{-1};(c) Ragone plot of energy density versus power density; (d) Capacitance retention over 10000 charge-discharge cycles at 10 A g^{-1}.

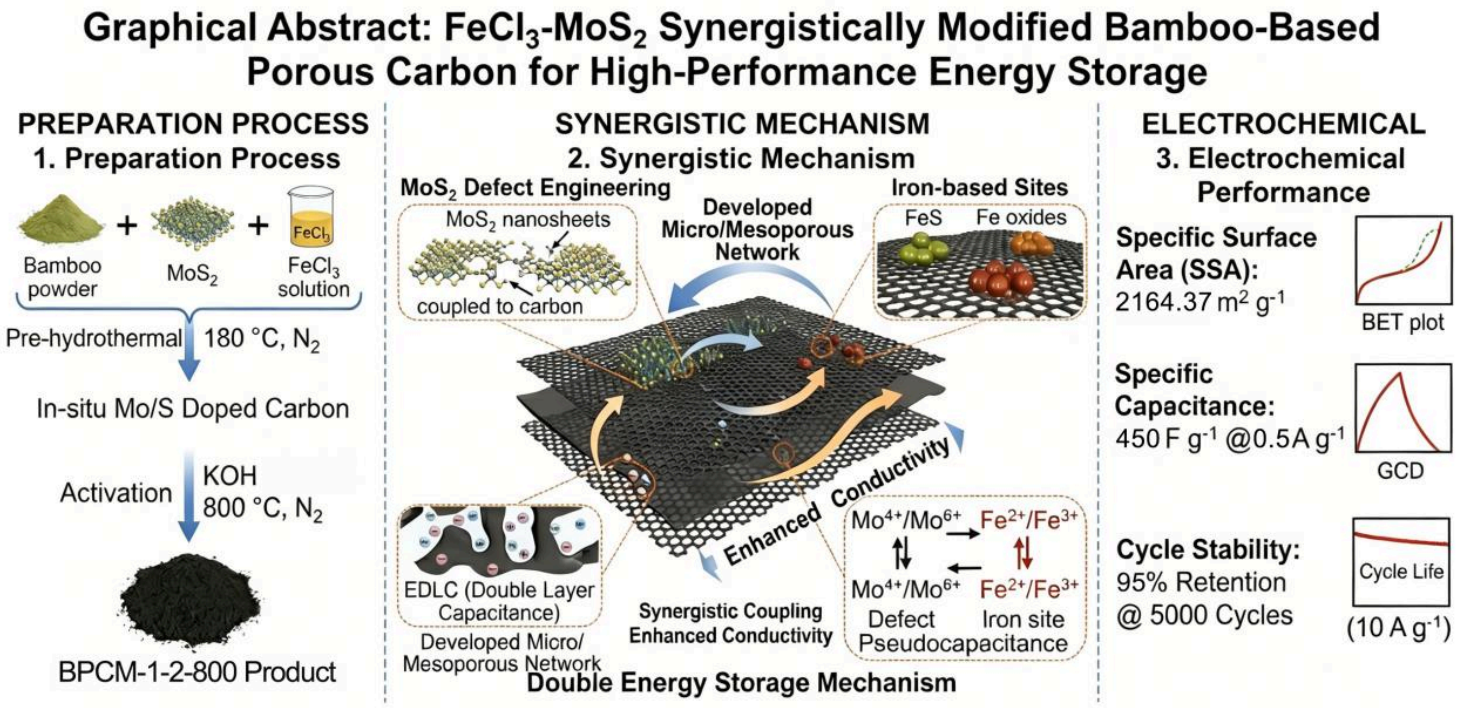

The synergistic coupling of $FeCl_3$-MoS_2 defect engineering, Fe-based pseudocapacitance, and hierarchical porous structure enhances the charge storage, ion transport, and stability of bamboo-based porous carbon electrodes.

Figure 10

Schematic illustration of the formation mechanism of $FeCl_3$-MoS_2 synergistically modified bamboo powder-based porous carbon.